Nanographenes

On-Surface Synthesis of Non-Benzenoid Nanographenes Embedding Azulene and Stone-Wales Topologies

Kalyan Biswas[+], Qifan Chen[+], Sebastian Obermann, Ji Ma,* Diego Soler-Polo,
Jason Melidonie, Ana Barragán, Ana Sánchez-Grande, Koen Lauwaet, José M. Gallego,
Rodolfo Miranda, David Écija,* Pavel Jelínek,* Xinliang Feng, and José I. Urgel*

Abstract: The incorporation of non-benzenoid motifs in graphene nanostructures significantly impacts their properties, making them attractive for applications in carbon-based electronics. However, understanding how specific non-benzenoid structures influence their properties remains limited, and further investigations are needed to fully comprehend their implications. Here, we report an on-surface synthetic strategy toward fabricating non-benzenoid nanographenes containing different combinations of pentagonal and heptagonal rings. Their structure and electronic properties were investigated via scanning tunneling microscopy and spectroscopy, complemented by computational investigations. After thermal activation of the precursor **P** on the Au(111) surface, we detected two major nanographene products. Nanographene $\mathbf{A_{a-a}}$ embeds two azulene units formed through oxidative ring-closure of methyl substituents, while $\mathbf{A_{a-s}}$ contains one azulene unit and one Stone-Wales defect, formed by the combination of oxidative ring-closure and skeletal ring-rearrangement reactions. $\mathbf{A_{a-a}}$ exhibits an antiferromagnetic ground state with the highest magnetic exchange coupling reported up to date for a non-benzenoid containing nanographene, coexisting with side-products with closed shell configurations resulted from the combination of ring-closure and ring-rearrangement reactions ($\mathbf{B_{a-a}}$, $\mathbf{B_{a-s}}$, $\mathbf{B_{s-a}}$ and $\mathbf{B_{s-s}}$). Our results provide insights into the single gold atom assisted synthesis of novel NGs containing non-benzenoid motifs and their tailored electronic/magnetic properties.

Introduction

Nanographenes (NGs) are nanometer-size polycyclic aromatic hydrocarbons (PAHs) with well-defined chemical structures.[1] These finite graphene segments comprise non-alternant ring topologies within their honeycomb lattice, resulting in extraordinary physicochemical properties.[2,3] The geometric confinement prevailing in NGs, as well as in graphene stripes named graphene nanoribbons,[4] holds potential for controllable band gaps, relevant for graphene-based electronics.

The incorporation of non-benzenoid rings in graphene nanostructures strongly influences their chemical and physical properties, such as electronic band gap, chemical reactivity, or magnetism, among others.[5–8] Therefore, an exhaustive study of well-defined non-benzenoid motifs in

[*] Dr. K. Biswas,[+] Dr. A. Barragán, Dr. A. Sánchez-Grande,
Dr. K. Lauwaet, Prof. R. Miranda, Prof. D. Écija, Dr. J. I. Urgel
IMDEA Nanoscience, C/Faraday 9, Campus de Cantoblanco, 28049
Madrid, Spain
E-mail: david.ecija@imdea.org
        jose-ignacio.urgel@imdea.org

Q. Chen,[+] Dr. D. Soler-Polo, Prof. P. Jelínek
Institute of Physics of the Czech Academy of Science, CZ-16253
Praha, Czech Republic
E-mail: jelinekp@fzu.cz

Q. Chen[+]
Faculty of Mathematics and Physics, Charles University, V Holešo-
vičkách 2, 18000 Praha, Czech Republic

S. Obermann, Dr. J. Ma, Dr. J. Melidonie, Prof. X. Feng
Center for Advancing Electronics Dresden (cfaed) & Faculty of
Chemistry and Food Chemistry, Technische Universität Dresden, D-
01069 Dresden, Germany
E-mail: ji.ma@tu-dresden.de

Dr. J. Ma, Prof. X. Feng
Max Planck Institute of Microstructure Physics, Weinberg 2, 06120
Halle, Germany

Dr. J. M. Gallego
Instituto de Ciencia de Materiales de Madrid (ICMM), CSIC,
Cantoblanco, 28049 Madrid, Spain

Prof. R. Miranda
Departamento de Física de la Materia Condensada, Universidad
Autónoma de Madrid, 28049 Madrid, Spain

Prof. D. Écija, Dr. J. I. Urgel
Unidad de Nanomateriales avanzados, IMDEA Nanoscience,
Unidad asociada al CSIC por el ICMM, 28049 Madrid, Spain

Prof. P. Jelínek
Regional Centre of Advanced Technologies and Materials, Palacký
University Olomouc, 77146 Olomouc, Czech Republic

[+] Equally contributing authors

graphene nanostructures, from both fundamental and applied perspectives, is crucial to elucidate their structure–property relationship. From the energetic perspective, pentagon-heptagon pairs (fused five-seven membered rings, so called azulene), structural isomers of naphthalene, are one of the most stable defect models induced by the rearrangement of carbon-carbon (C–C) bonds.[9–11] Such intrinsic topological defects in graphene nanostructures are frequently classified according to dimensionality, where point Stone–Wales defects (0D), azulene dislocations (1D) and chains in grain boundaries (2D) are among the most recognized defects.[12]

Nevertheless, one of the main challenges limiting the study of non-benzenoid molecules is their difficult synthesis and separation, and only a few examples have been successfully reported.[9–11,13–22] In contrast, the "bottom-up" approach, combining modern solutions and on-surface syntheses to create NGs with atomically precise edge structures, has recently appeared as an alternative.[23]

Over the last decade, the field of on-surface chemistry has experienced a great progress, with the successful achievement of a plethora of advanced metal-catalyzed on-surface reactions unattainable through solution chemistry.[24] This approach has proven to be highly effective in synthesizing a wide range of NGs on noble metal surfaces, including periacenes,[25–29] cycloarenes,[30,31] rhombene-shaped,[32,33] or skeletal ring-rearranged NGs.[33–39] In this regard, recent efforts have been focused on synthesizing and characterizing NGs with an open-shell (magnetic) ground state, as they hold potential for next-generation quantum technology.[40] However, up to date, the realization of atomically precise open-shell non-benzenoid NGs remains limited,[41–44,64] and the role of non-alternant topologies in tailoring their structural, optical, electronic, and magnetic properties is still far from being fully understood.[45–54]

In this work, we report a comprehensive study on the on-surface generation of NGs embedding azulene and Stone-Wales topologies synthesized on a coinage metal surface under ultra-high vacuum (UHV) conditions. Scanning tunneling microscopy (STM) measurements reveal the formation of distinct NGs, which undergo oxidative ring-closure of the methyl substituents, ring-rearrangement reactions, and their combination through thermal activation on the Au(111) surface. Our molecular-level investigations demonstrate that NGs A_{a-a} and B_{a-a} contain two azulene units in their polycyclic framework, A_{a-s}, B_{a-s} and B_{s-a} accommodate one azulene unit and one Stone-Wales defect. At the same time, B_{s-s} possess two Stone-Wales defects (see Scheme 1). Such findings are complemented by free-energy quantum mechanics/molecular mechanics (QM/MM) calculations, which provide a rationalization of the mechanisms driving the distinct reaction pathways. In addition to our detailed chemical and structural studies, scanning tunneling spectroscopy (STS) measurements, along with density func-
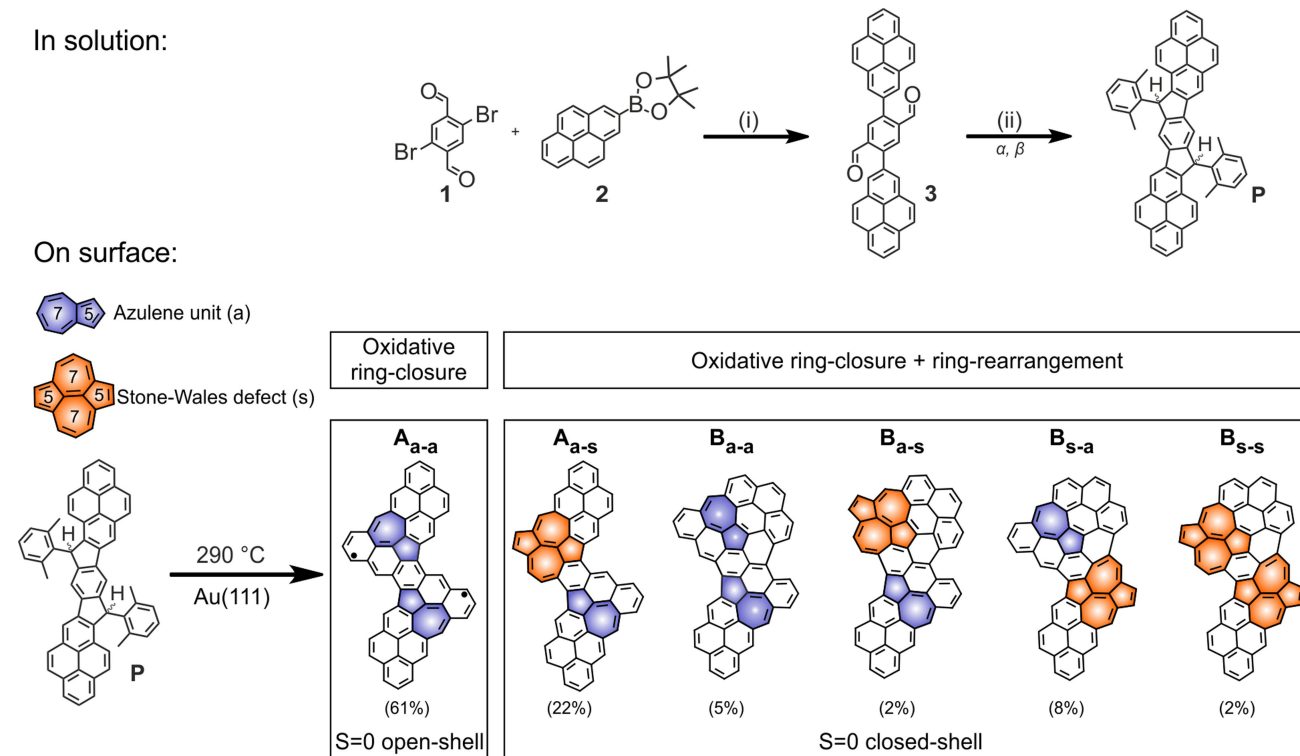
Scheme 1. In-solution and on-surface synthetic routes toward the formation of NGs with embedded azulene and Stone-Wales defects. Reagents and conditions for the solution synthesis: (i) Pd(PPh₃)₄, K₂CO₃, toluene, ethanol, H₂O, 90 °C, overnight, 70 %. (ii) α. 2,6-dimethylphenylmagnesiumbromide, tetrahydrofuran, RT, 30 mins; β. BF₃·OEt₂, dichloromethane, RT, 5 mins, 65 % in two steps. The azulene units formed via oxidative ring-closure are marked by non-benzenoid rings colored in purple, while the Stone-Wales defects resulting from ring-rearrangement reactions are indicated by red-colored rings.

tional theory (DFT) as well as many-body complete active space-configuration interaction (CAS-CI) calculations, unravel their electronic structure. **A$_{a-a}$** possesses an antiferromagnetic (open-shell singlet) ground state with a remarkably high magnetic exchange coupling (J$_{eff}$=180 mV), whereas the other synthesized NGs present a closed-shell configuration. The NGs reported herein shed light on the synthesis of graphene nanostructures with non-alternant ring topologies and significant insights regarding their electronic and magnetic properties.

Results and Discussion

As a starting point, the pyrene-fused *s*-indacene dihydro precursor (**P**) with two embedded dimethylphenyl groups was synthesized in solution, as shown in Scheme 1. First, Suzuki coupling reaction between the readily prepared 2,5-dibromoterephthalaldehyde (**1**) and 4,4,5,5-tetramethyl-2-(pyren-2-yl)-1,3,2-dioxaborolane (**2**) gave the 2,5-di(pyren-2-yl)terephthalaldehyde intermediate (**3**) with a yield of 70%. Subsequently, compound **3** was treated with 2,6-dimethylphenylmagnesiumbromide to afford the diol intermediate, which was directly subjected to an intramolecular Friedel–Crafts alkylation promoted by BF$_3$·OEt$_2$, yielding the target dihydro precursor **P** in 65% yield over two steps (see general methods and materials in the Supporting Information). To investigate the on-surface reactions of **P**, a submonolayer coverage was then deposited onto a pristine Au(111) surface held at room temperature (RT) in an UHV environment. STM imaging of the sample provided evidence of self-assembled nanostructures that contain nonplanar segments resulting from the steric hindrance between the methyl groups and the molecular backbone, which suggests that **P** adsorbs intact onto the surface (see Figure S1). Annealing the sample to 290°C led to significant changes in the STM images. Figure 1a demonstrates the coexistence of individual and planar NGs alongside a few fused nanostructures. We note that, within the individual and planar species, a majority (~80%) presents a symmetric "Z-shape", named NGs **A** (Figure 1a). Specifically, a statistical analysis of the reaction products (see Scheme 1) based on more than 300 NGs, shows that there are two different Z-shaped NGs (**A$_{a-a}$** and **A$_{a-s}$**). **A$_{a-a}$** is the majority of the NGs formed on the surface (61%), while **A$_{a-s}$** is less commonly observed (22%).

First, we have studied the chemical structure of **A$_{a-a}$**, acquiring a topographic STM image (Figure 1b) and its corresponding constant-height high-resolution STM image, obtained using a carbon monoxide (CO) functionalized tip and recorded in the Pauli repulsion regime (Figure 1c).[55] Figure 1d depicts the corresponding structural formula of **A$_{a-a}$**, clearly revealing the presence of two azulene units in the molecular backbone.

This is a direct consequence of the successful oxidative ring-closure of the four methyl substituents, which results in the formation of two heptagonal and two hexagonal rings integrated into the NG, highlighted by white and purple arrows, respectively.

Subsequently, we investigated its electronic properties by conducting STS measurements. Our results indicate that for **A$_{a-a}$** (Figure 1e–h), the local density of states (LDOS) exhibits resonances at −870 mV, −380 mV, 410 mV, and 780 mV, as revealed by the differential conductance (dI/dV vs V) spectra obtained using a CO-functionalized tip (Figure 1e). We have obtained experimental constant-current dI/dV maps at the energies mentioned above, which display the agreement with the simulated dI/dV maps of the HOMO−1, SOMO (singly occupied molecular orbital), SUMO (singly unoccupied molecular orbital), and LUMO+1 molecular orbitals for a free-standing **A$_{a-a}$** (as depicted in Figure 1f). Based on the energy separation between the SOMO and SUMO, we determined an experimental Coulomb gap of 790 meV. Upon a closer examination of the energy region near the Fermi level (Figure 1g), an abrupt stepwise change in conductance that is symmetric around the Fermi energy at ±180 meV is observed. This behavior indicates an inelastic excitation and the threshold of the effective exchange parameter (J$_{eff}$), which is extracted from the d^2I/dV^2 spectrum in Figure 1h. This inelastic excitation and the presence of singly occupied MOs provide strong evidence for **A$_{a-a}$**'s open-shell ground state. Such an inelastic excitation is assigned to a singlet−triplet magnetic excitation (S=0 to S=1; Figure 1i) resulting from tunneling electrons, in good agreement with the calculated J$_{eff}$=208 mV (obtained through the many-body DFT+CASCI method, see methods and Figure S3 in the Supporting Information), representing to the best of our knowledge, the highest magnetic exchange coupling reported for a non-benzenoid-containing NG to date.[32,33] Finally, Figure 1j depicts spin-polarized DFT calculations of the free-standing NG, showing the spin density distribution of the molecule.

The ability of the Au(111) surface to catalyze chemical reactions involved in the formation of molecular carbon-based nanostructures is nowadays widely recognized.[23,56] Such surface-catalyzed reactions significantly reduce the strength of the C–X bonds (X=C, H, halogens, etc.), often leading to the selective cleavage of X and the generation of novel nanostructures. Furthermore, the cleavage of C–H bonds in aromatic complexes is a non-trivial matter and requires high activation energies.[57,58] In fact, recent studies have shown the significant role of gold adatoms in enabling a significant reduction of activation energies in the cleavage of C–H and C–C bonds in PAH molecular compounds on surfaces.[54,59]

Therefore, to gain a more comprehensive understanding of the reaction mechanism, we have explored the reaction pathway leading to the formation of **A$_{a-a}$** using DFT and Umbrella Sampling quantum mechanics/molecular mechanics (QM/MM) simulations[60] at 227°C. To rationalize the different reaction pathways from the precursor **P** to the final nanographene **A$_{a-a}$**, we need to take into account several reaction steps, including a series of selective dehydrogenation reactions, as well as the closure and planarization of the rings (see Figure S2 for the structural formula of the complete sequence of dehydrogenation reactions from **P** to the final state (**FS**), also named **A$_{a-a}$**). To reduce the computational cost, we have focused our theoretical studies
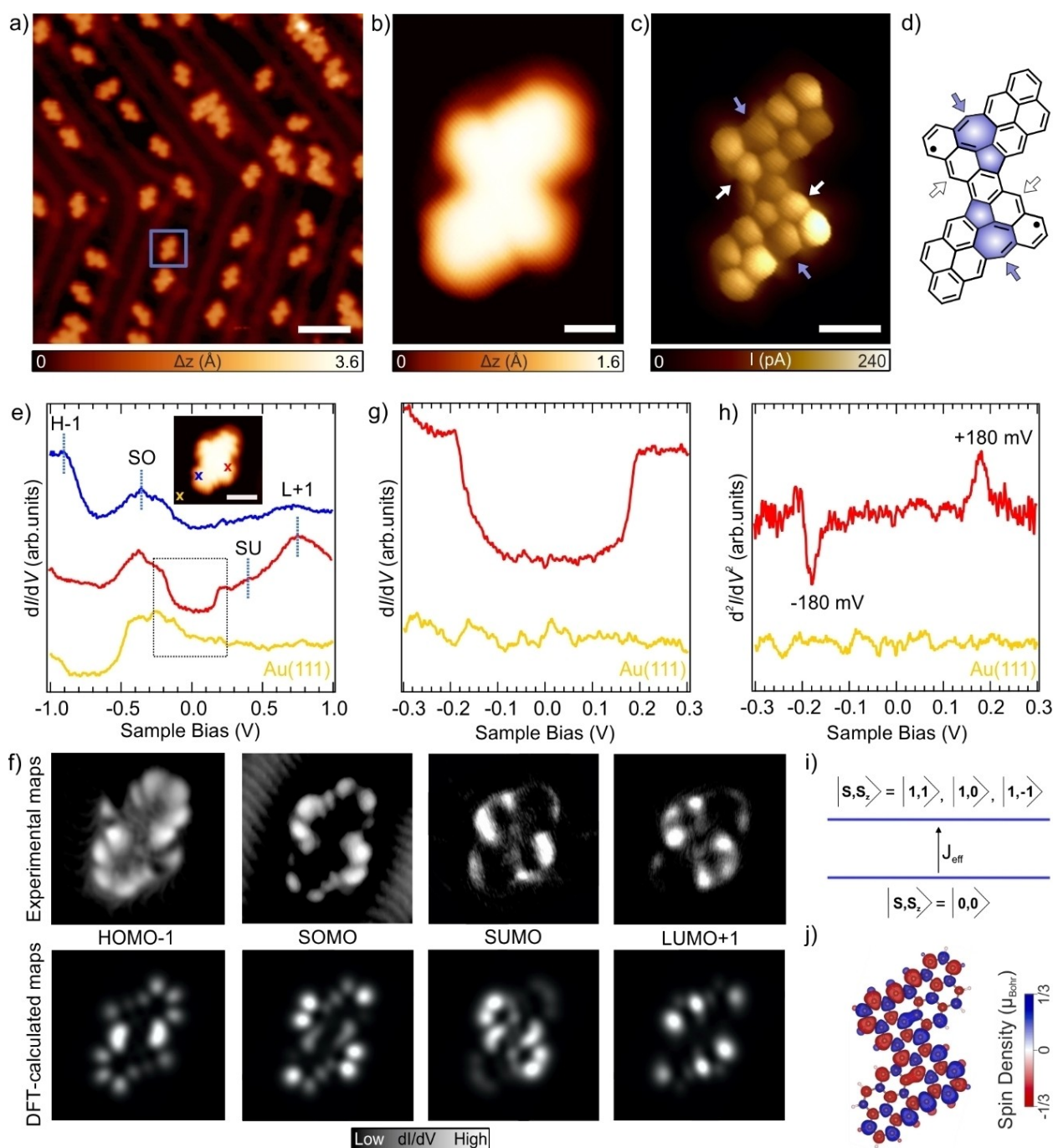
Figure 1. Structural and electronic characterization of the non-benzenoid nanographene A_{a-a} on Au(111). a) Overview STM topographic image of the surface after the deposition of **P** and subsequent annealing at 290 °C, which led to intramolecular oxidative ring-closure and formation of different reaction products. Scanning parameters: $V_b = 200$ mV, $I_t = 120$ pA, scale bar 5 nm. The blue-colored square highlights a nanographene A_{a-a}. b) Zoomed-in STM image of an isolated NG A_{a-a}. Scanning parameters: $V_b = 5$ mV, $I_t = 50$ pA, scale bar = 0.5 nm. c) Constant-height high-resolution STM image of (b) acquired with a CO-functionalized tip that reveals the chemical structure of the NG. Scanning parameters: $Z_{offset} = 180$ pm above STM set point: 5 mV, 50 pA, scale bar = 0.5 nm. d) Structural formula of A_{a-a}. Purple and white arrows highlight the formation of a heptagonal and a hexagonal ring, respectively. e) dI/dV spectroscopy on A_{a-a}. Acquisition positions are marked with corresponding filled color cross in the inset STM image. The orange curve corresponds to the reference dI/dV spectrum acquired on Au(111). f) Constant-current dI/dV maps (top) and the corresponding simulated DFT maps (bottom) of the HOMO−1 (H-1), SOMOs (SO), SUMOs (SU), and LUMO+1 (L+1) of A_{a-a}. Scanning parameters: (H-1), $V_b = -0.87$ V, $I_t = 200$ pA; (SO), $V_b = -0.38$ V, $I_t = 250$ pA; (SU), $V_b = 0.41$ V, $I_t = 250$ pA; (L+1), $V_b = 0.78$ V, $I_t = 200$ pA. g) Zoomed-in differential conductance spectra in the bias range marked with the box in (e), where an abrupt stepwise change in conductance around the Fermi energy is observed. h) d^2I/dV^2 spectra of (g). i) Schematic representation of the ground- and first-excited states. S_z denotes the spin projection quantum number. j) Calculated spin density distribution of a free-standing A_{a-a} NG using DFT-PBE0.
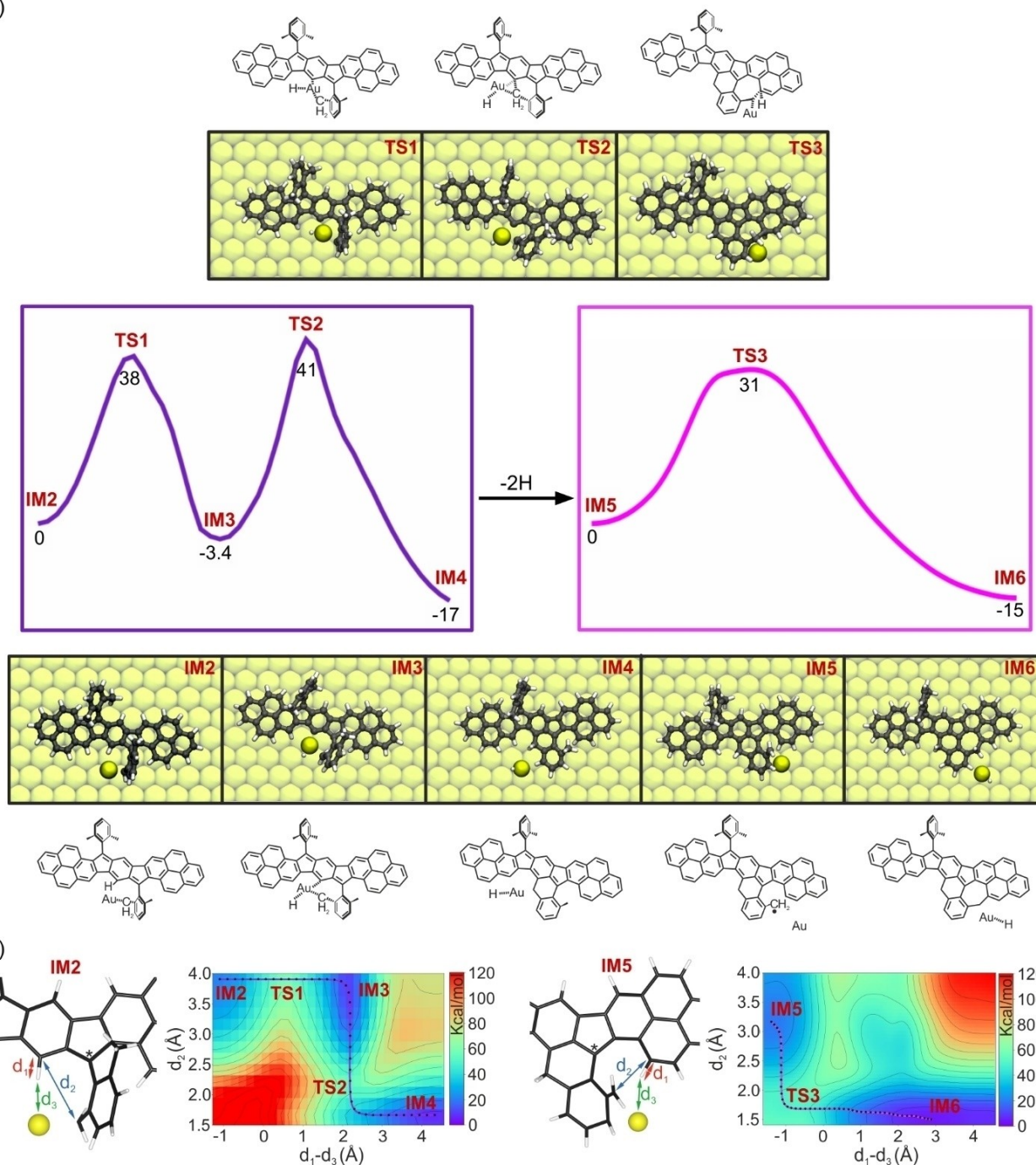
Figure 2. QM/MM free energy calculation and maps of the gold adatom-assisted formation of the two new carbon-carbon bonds toward the formation of product **A**$_{a-a}$. a) Structural formulae and corresponding top view of the reaction snapshots representing the intermediate states (IM) and transition states (TS) involve in the formation of new carbon-carbon bonds evaluated at 227 °C, together with the free energy profile of the three-step reaction associated with the formation of the two new carbon-carbon bonds. C, H and Au are represented in black, white and yellow balls, respectively. Free energy profile values are given in Kcal/mol. b) Zoomed-in schemes of the molecule showing the reaction coordinates employed in the free energy maps (a). Carbon-carbon distance (d_2) is highlighted by a blue arrow, and the difference between the hydrogen-carbon distance (d_1, red arrow) and the hydrogen-adatom distance (d_3, green arrow). The asterisk serves as a guide to the eye for comparing both molecules. In addition, the two-dimensional weighted histogram analysis method (2D-WHAM) free energy maps for the closure of the rings in two stages is also shown. The first map depicts the most favorable reaction pathway for **IM2** to **IM4** and the second one for **IM5** to **IM6**; in both cases we have employed the reaction coordinates, described in (b). Notice that to go from **IM4** to **IM5** an extra hydrogen from the methyl group has been removed, so that the second ring-closure can initiate (see Supporting Information for further information). For detailed atomistic view of the optimal reaction pathways shown in (b) see videos attached in the Supporting Information.
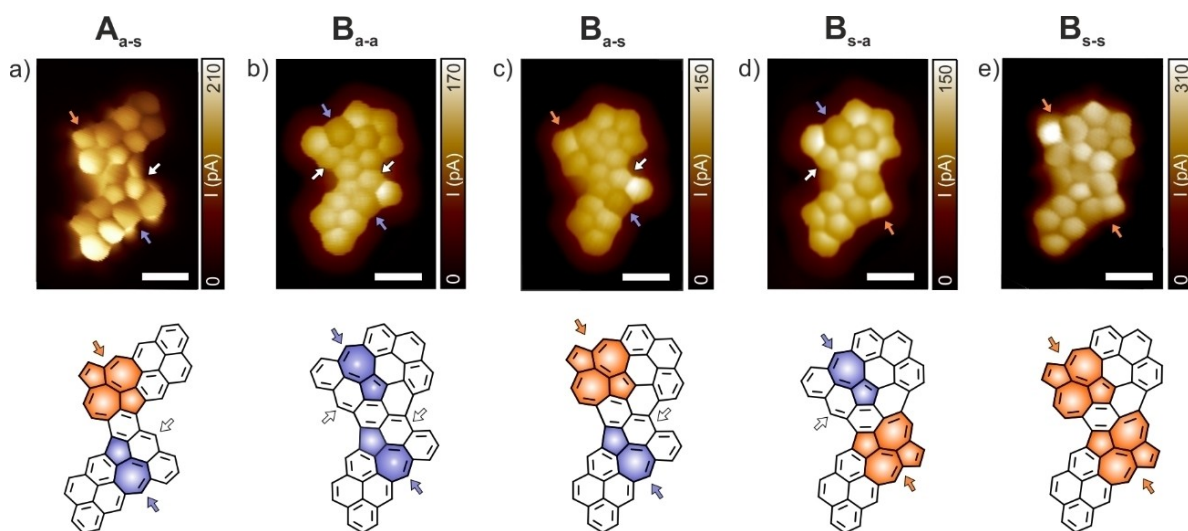
Figure 3. Structural characterization of A_{a-s}, B_{a-a}, B_{a-s}, B_{s-a} and B_{s-s} NGs on Au(111). a–e) Constant-height high-resolution STM images acquired with a CO-functionalized tip and corresponding structural formulae of individual A_{a-s}, B_{a-a}, B_{a-s}, B_{s-a} and B_{s-s} NGs upon annealing of the sample at 290°C. Scanning parameters: $V_b = 5$ mV, $I_t = 50$ pA, $Z_{offset} = 100$ pm, 95 pm, 90 pm, 90 pm and 90 pm, respectively. All scale bars = 0.5 nm. The colored arrows depicted in the structural formulae serve to highlight the formation of new rings. Azulene subunits are highlighted in purple and Stone-Wales defects in red.

on only one of the two identical reaction sites (lower segment of the NG in Figure 2a). Based on reported literature,[61,62] we have also considered that the hydrogen atoms situated at the sp^3 carbon atoms of the two five-membered rings are already detached from **P** (denoted as the initial state (**IS**) in Figure S2), once the molecule is deposited on Au(111) surface. In the second step, the dehydrogenation of the methyl group, corresponding to steps **IS→IM1**, occurs. According to our calculations, the dehydrogenation assisted by a single gold adatom has a very low barrier ~17 kcal/mol (see Table S1 for a comparison with other less favorable gold adatom-assisted dehydrogenations and C–C bond cleavage previous to the ring-closure process). Importantly, a single gold adatom substantially lowers the activation barrier and stabilizes the final product energetically by passivation of the radical carbon atom generated after the dehydrogenation.

Figure 2 displays the two key steps in the formation of A_{a-a}, namely the single gold adatom-assisted formation of two new carbon-carbon bonds, comprising the intermediate and transition steps from **IM2** to **IM6** and from **TS1** to **TS3**, respectively. In addition, the corresponding optimal activation energy profiles between such steps are summarized in Figure 2a. We have studied these two processes by means of two independent reaction coordinates defined in terms of atomic bond lengths d_1, d_2 and d_3, which makes the simulations computationally extensive. The two-dimensional (2D) maps shown in Figure 2b depict an intuitive way to plot the minimum energy pathways for energy landscapes.[63] The optimal reaction pathways presented in Figure 2b are also summarized in the videos attached in the Supporting Information.

In the first step, a feasible scenario is the one where a gold adatom breaks the C–H bond on an adjacent benzene ring, which facilitates the formation of a new benzene ring

(see reaction path **IM2→IM4** in Figure 2a). Notice that, to describe the transition from **IM2** to **IM4**, two reaction coordinates, d_2 and d_1–d_3, are employed simultaneously (see Figure 2b). According to our QM/MM calculations, this sequence has a relatively low activation energy barrier 35–45 kcal/mol, which allows the reaction to occur within a matter of seconds at the experimental temperature 290°C. Importantly, the formed intermediates are thermodynamically more stable than the initial intermediate **IM1**. Next, another gold-assisted dehydrogenation step of the other methyl group takes place, forming intermediate **IM5**. Afterward, the cyclization process leading to a heptagonal ring (**IM6**) can be achieved with a relatively favorable activation barrier of 31 kcal/mol. An identical gold-assisted formation of two new carbon-carbon bonds is expected to occur also at the other side of the precursor, see Figure S2. To form the final nanographene A_{a-a}, both the pentagonal and heptagonal rings must dehydrogenate the remaining sp^3 carbons (see Figure S4 in the Supporting Information). Moreover, Figure S4 also compares the free energy profile of the dehydrogenation process with and without a single gold adatom, which underlines the importance of the gold adatoms, as discussed previously. Note that from the calculations, we cannot determine the order in which the dehydrogenations and closure of the remaining rings occur.

Finally, we have investigated the minority NGs found on the Au(111) surface. A_{a-s} exhibits a slight asymmetry with respect to the "Z-shape" compared with the STM topography of A_{a-a}. A close inspection of A_{a-s} is shown in Figure 3a. It unveils a skeletal ring-rearrangement reaction that gives rise to a unique combination of pentagonal and heptagonal rings at one of the reacting sites of the NG, identified as a Stone–Wales defect (highlighted by red arrows). The formation of A_{a-s} implies a 1,2-shift of a carbon-carbon bond adjacent to the embedded azulene unit,

reducing the ring size of a hexagon to a pentagon while extending another to a heptagon (see Figure S5). In addition, a non-negligible amount of asymmetric NGs, named **B**, were also achieved (13 %). Figures 3b–e show the four different NGs detected on the surface. Herein, an unforeseen rearrangement of one pyrene subunit per nanographene is observed in all of them, followed by the oxidative ring-closure of methyl substituents and/or the combination of oxidative ring-closure and skeletal ring-rearrangement reactions that give rise to the formation of the azulene or Stone-Wales defects, respectively (see the details in Figure S5). Therefore, the combination of the above-mentioned reactions induces the formation of four distinct **B** type NGs containing: i) two azulene units formed through oxidative ring-closure of methyl substituents (B_{a-a}, in Figure 3b), ii) one azulene unit and one Stone-Wales defect, formed by the combination of oxidative ring-closure and a skeletal ring-rearrangement reaction that occurs at one side of the NG (B_{a-s} and B_{s-a}, in Figure 3c, d), and iii) two Stone–Wales defects, produced by oxidative ring-closure and skeletal ring-rearrangement that arises at the two sides of the NG (B_{s-s}, in Figure 3e). Furthermore, the electronic structure of the five NGs shown in Figure S6 reveals a non-magnetic, i.e. closed-shell ground state where the abrupt stepwise change in conductance symmetric with respect to the Fermi Energy is absent, in contrasts to what has been observed for A_{a-a}.

Conclusion

In summary, we explored the on-surface generation of NGs embedding azulene and Stone-Wales topologies synthesized on a coinage-metal surface under UHV conditions. The reported NGs contain two azulene units (A_{a-a}, B_{a-a}), one azulene unit, one Stone-Wales defect (A_{a-s}, B_{a-s} and B_{s-a}) and two Stone-Wales defects (B_{s-s}). The majority product, A_{a-a}, is formed via oxidative ring-closure of the four methyl substituents of the employed precursor after annealing of the sample, whether all the other NGs undergo oxidative ring-closure and skeletal ring-rearrangement reactions. Their structural characterization has been detailed by high-resolution STM imaging. STS measurements, complemented with state-of-the-art theoretical calculations, reveal that A_{a-a} possesses an antiferromagnetic open-shell singlet ground state with a remarkably high magnetic exchange coupling (the highest among the reported non-benzenoid-containing NGs); in contrast, the other NGs present a closed-shell configuration. Finally, DFT and QM/MM simulations provide insights into the reaction mechanism that originates A_{a-a}, revealing the fundamental catalytic role of the single gold adatoms for oxidative ring-closure. This observation opens new venues to explore single-adatom gold catalysis in on-surface synthesis.

Conflict of Interest

The authors declare no conflict of interest.

Data Availability Statement

The data that support the findings of this study are available from the corresponding author upon reasonable request.

Keywords: Nanographenes · Azulene and Stone-Wales defects · Scanning tunnelling microscopy · Open-shell species · Oxidative ring-closure

[1] A. Narita, in *Synthetic Methods for Conjugated Polymers and Carbon Materials* (Eds.: M. Leclerc, J.-F. Morin), Wiley-VCH Verlag GmbH & Co. KGaA, Weinheim, Germany, **2017**, pp. 183–228.

[2] A. Narita, X.-Y. Wang, X. Feng, K. Müllen, *Chem. Soc. Rev.* **2015**, *44*, 6616–6643.

[3] J. Wu, W. Pisula, K. Müllen, *Chem. Rev.* **2007**, *107*, 718–747.

[4] Y. Gu, Z. Qiu, K. Müllen, *J. Am. Chem. Soc.* **2022**, *144*, 11499–11524.

[5] H. I. Rasool, C. Ophus, A. Zettl, *Adv. Mater.* **2015**, *27*, 5771–5777.

[6] J. Hong, C. Jin, J. Yuan, Z. Zhang, *Adv. Mater.* **2017**, *29*, 1606434.

[7] H. Xin, B. Hou, X. Gao, *Acc. Chem. Res.* **2021**, *54*, 1737–1753.

[8] X.-S. Zhang, Y.-Y. Huang, J. Zhang, W. Meng, Q. Peng, R. Kong, Z. Xiao, J. Liu, M. Huang, Y. Yi, L. Chen, Q. Fan, G. Lin, Z. Liu, G. Zhang, L. Jiang, D. Zhang, *Angew. Chem. Int. Ed.* **2020**, *59*, 3529–3533.

[9] Y. Fei, J. Liu, *Adv. Sci.* **2022**, *9*, 2201000.

[10] Y. Fei, Y. Fu, X. Bai, L. Du, Z. Li, H. Komber, K.-H. Low, S. Zhou, D. L. Phillips, X. Feng, J. Liu, *J. Am. Chem. Soc.* **2021**, *143*, 2353–2360.

[11] J. Ma, Y. Fu, E. Dmitrieva, F. Liu, H. Komber, F. Hennersdorf, A. A. Popov, J. J. Weigand, J. Liu, X. Feng, *Angew. Chem. Int. Ed.* **2020**, *59*, 5637–5642.

[12] F. Banhart, J. Kotakoski, A. V. Krasheninnikov, *ACS Nano* **2011**, *5*, 26–41.

[13] K. Kawasumi, Q. Zhang, Y. Segawa, L. T. Scott, K. Itami, *Nat. Chem.* **2013**, *5*, 739–744.

[14] Y. Segawa, H. Ito, K. Itami, *Nat. Rev. Mater.* **2016**, *1*, 15002.

[15] J. Wang, F. G. Gámez, J. Marín-Beloqui, A. Diaz-Andres, X. Miao, D. Casanova, J. Casado, J. Liu, *Angew. Chem. Int. Ed.* **2023**, *62*, e202217124.

[16] J. Liu, A. Narita, S. Osella, W. Zhang, D. Schollmeyer, D. Beljonne, X. Feng, K. Müllen, *J. Am. Chem. Soc.* **2016**, *138*, 2602–2608.

[17] J. Liu, S. Osella, J. Ma, R. Berger, D. Beljonne, D. Schollmeyer, X. Feng, K. Müllen, *J. Am. Chem. Soc.* **2016**, *138*, 8364–8367.

[18] N. Ogawa, Y. Yamaoka, H. Takikawa, K. Yamada, K. Takasu, *J. Am. Chem. Soc.* **2020**, *142*, 13322–13327.

[19] J. Borstelmann, J. Bergner, F. Rominger, M. Kivala, *Angew. Chem. Int. Ed.* **2023**, *62*, e202312740.

[20] S. Frisch, C. Neiß, S. Lindenthal, N. F. Zorn, F. Rominger, A. Görling, J. Zaumseil, M. Kivala, *Chem. Eur. J.* **2023**, *29*, e202203101.

[21] B. P. Klein, L. Ruppenthal, S. J. Hall, L. E. Sattler, S. M. Weber, J. Herritsch, A. Jaegermann, R. J. Maurer, G. Hilt, J. M. Gottfried, *ChemPhysChem* **2021**, *22*, 1065–1073.

[22] P. Liu, X.-Y. Chen, J. Cao, L. Ruppenthal, J. M. Gottfried, K. Müllen, X.-Y. Wang, *J. Am. Chem. Soc.* **2021**, *143*, 5314–5318.

[23] Q. Shen, H.-Y. Gao, H. Fuchs, *Nano Today* **2017**, *13*, 77–96.

[24] S. Clair, D. G. de Oteyza, *Chem. Rev.* **2019**, *119*, 4717–4776.

[25] S. Mishra, T. G. Lohr, C. A. Pignedoli, J. Liu, R. Berger, J. I. Urgel, K. Müllen, X. Feng, P. Ruffieux, R. Fasel, *ACS Nano* **2018**, *12*, 11917–11927.

[26] A. Sánchez-Grande, J. I. Urgel, L. Veis, S. Edalatmanesh, J. Santos, K. Lauwaet, P. Mutombo, J. M. Gallego, J. Brabec, P. Beran, D. Nachtigallová, R. Miranda, N. Martín, P. Jelínek, D. Écija, *J. Phys. Chem. Lett.* **2020**, 330–336.

[27] C. Rogers, C. Chen, Z. Pedramrazi, A. A. Omrani, H.-Z. Tsai, H. S. Jung, S. Lin, M. F. Crommie, F. R. Fischer, *Angew. Chem. Int. Ed.* **2015**, *54*, 15143–15146.

[28] K. Biswas, J. I. Urgel, M. R. Ajayakumar, J. Ma, A. Sánchez-Grande, S. Edalatmanesh, K. Lauwaet, P. Mutombo, J. M. Gallego, R. Miranda, P. Jelínek, X. Feng, D. Écija, *Angew. Chem. Int. Ed.* **2022**, *61*, e202114983.

[29] X.-Y. Wang, T. Dienel, M. Di Giovannantonio, G. B. Barin, N. Kharche, O. Deniz, J. I. Urgel, R. Widmer, S. Stolz, L. H. De Lima, M. Muntwiler, M. Tommasini, V. Meunier, P. Ruffieux, X. Feng, R. Fasel, K. Müllen, A. Narita, *J. Am. Chem. Soc.* **2017**, *139*, 4671–4674.

[30] M. Di Giovannantonio, X. Yao, K. Eimre, J. I. Urgel, P. Ruffieux, C. A. Pignedoli, K. Müllen, R. Fasel, A. Narita, *J. Am. Chem. Soc.* **2020**, *142*, 12046–12050.

[31] Q. Fan, D. Martin-Jimenez, S. Werner, D. Ebeling, T. Koehler, T. Vollgraff, J. Sundermeyer, W. Hieringer, A. Schirmeisen, J. M. Gottfried, *J. Am. Chem. Soc.* **2020**, *142*, 894–899.

[32] S. Mishra, X. Yao, Q. Chen, K. Eimre, O. Gröning, R. Ortiz, M. Di Giovannantonio, J. C. Sancho-García, J. Fernández-Rossier, C. A. Pignedoli, K. Müllen, P. Ruffieux, A. Narita, R. Fasel, *Nat. Chem.* **2021**, *13*, 581–586.

[33] K. Biswas, D. Soler, S. Mishra, Q. Chen, X. Yao, A. Sánchez-Grande, K. Eimre, P. Mutombo, C. Martín-Fuentes, K. Lauwaet, J. M. Gallego, P. Ruffieux, C. A. Pignedoli, K. Müllen, R. Miranda, J. I. Urgel, A. Narita, R. Fasel, P. Jelínek, D. Écija, *J. Am. Chem. Soc.* **2023**, *145*, 2968–2974.

[34] A. Shiotari, T. Nakae, K. Iwata, S. Mori, T. Okujima, H. Uno, H. Sakaguchi, Y. Sugimoto, *Nat. Commun.* **2017**, *8*, 16089.

[35] N. Pavliček, P. Gawel, D. R. Kohn, Z. Majzik, Y. Xiong, G. Meyer, H. L. Anderson, L. Gross, *Nat. Chem.* **2018**, *10*, 853–858.

[36] B. Schuler, S. Fatayer, F. Mohn, N. Moll, N. Pavliček, G. Meyer, D. Peña, L. Gross, *Nat. Chem.* **2016**, *8*, 220–224.

[37] F. Albrecht, S. Fatayer, I. Pozo, I. Tavernelli, J. Repp, D. Peña, L. Gross, *Science* **2022**, *377*, 298–301.

[38] B. Mallada, B. De la Torre, J. I. Mendieta-Moreno, D. Nachtigallová, A. Matěj, M. Matoušek, P. Mutombo, J. Brabec, L. Veis, T. Cadart, M. Kotora, P. Jelínek, *J. Am. Chem. Soc.* **2021**, *143*, 14694–14702.

[39] T. G. Lohr, J. I. Urgel, K. Eimre, J. Liu, M. Di Giovannantonio, S. Mishra, R. Berger, P. Ruffieux, C. A. Pignedoli, R. Fasel, X. Feng, *J. Am. Chem. Soc.* **2020**, *142*, 13565–13572.

[40] S. Song, J. Su, M. Telychko, J. Li, G. Li, Y. Li, C. Su, J. Wu, J. Lu, *Chem. Soc. Rev.* **2021**, *50*, 3238–3262.

[41] S. Mishra, M. Krzeszewski, C. A. Pignedoli, P. Ruffieux, R. Fasel, D. T. Gryko, *Nat. Commun.* **2018**, *9*, 1714.

[42] J. Liu, S. Mishra, C. A. Pignedoli, D. Passerone, J. I. Urgel, A. Fabrizio, T. G. Lohr, J. Ma, H. Komber, M. Baumgarten, C. Corminboeuf, R. Berger, P. Ruffieux, K. Müllen, R. Fasel, X. Feng, *J. Am. Chem. Soc.* **2019**, *141*, 12011–12020.

[43] K. Biswas, L. Yang, J. Ma, A. Sánchez-Grande, Q. Chen, K. Lauwaet, J. M. Gallego, R. Miranda, D. Écija, P. Jelínek, X. Feng, J. I. Urgel, *Nanomaterials* **2022**, *12*, 224.

[44] S. Mishra, D. Beyer, R. Berger, J. Liu, O. Gröning, J. I. Urgel, K. Müllen, P. Ruffieux, X. Feng, R. Fasel, *J. Am. Chem. Soc.* **2020**, *142*, 1147–1152.

[45] Q. Fan, L. Yan, M. W. Tripp, S. R. Kachel, M. Chen, A. S. Foster, U. Koert, P. Liljeroth, J. M. Gottfried, *Science* **2021**, *372*, 852–856.

[46] B. P. Klein, S. E. Harman, L. Ruppenthal, G. M. Ruehl, S. J. Hall, S. J. Carey, J. Herritsch, M. Schmid, R. J. Maurer, R. Tonner, C. T. Campbell, J. M. Gottfried, *Chem. Mater.* **2020**, *32*, 1041–1053.

[47] Q. Fan, D. Martin-Jimenez, D. Ebeling, C. K. Krug, L. Brechmann, C. Kohlmeyer, G. Hilt, W. Hieringer, A. Schirmeisen, J. M. Gottfried, *J. Am. Chem. Soc.* **2019**, *141*, 17713–17720.

[48] I. C.-Y. Hou, Q. Sun, K. Eimre, M. Di Giovannantonio, J. I. Urgel, P. Ruffieux, A. Narita, R. Fasel, K. Müllen, *J. Am. Chem. Soc.* **2020**, *142*, 10291–10296.

[49] J. I. Urgel, M. Di Giovannantonio, Y. Segawa, P. Ruffieux, L. T. Scott, C. A. Pignedoli, K. Itami, R. Fasel, *J. Am. Chem. Soc.* **2019**, *141*, 13158–13164.

[50] J. I. Urgel, M. D. Giovannantonio, K. Eimre, T. G. Lohr, J. Liu, S. Mishra, Q. Sun, A. Kinikar, R. Widmer, S. Stolz, M. Bommert, R. Berger, P. Ruffieux, C. A. Pignedoli, K. Müllen, X. Feng, R. Fasel, *Angew. Chem. Int. Ed.* **2020**, *132*, 13383–13389.

[51] L. Qin, Y.-Y. Huang, B. Wu, J. Pan, J. Yang, J. Zhang, G. Han, S. Yang, L. Chen, Z. Yin, Y. Shu, L. Jiang, Y. Yi, Q. Peng, X. Zhou, C. Li, G. Zhang, X.-S. Zhang, K. Wu, D. Zhang, *Angew. Chem. Int. Ed.* **2023**, *62*, e202304632.

[52] D. Skidin, F. Eisenhut, M. Richter, S. Nikipar, J. Krüger, D. A. Ryndyk, R. Berger, G. Cuniberti, X. Feng, F. Moresco, *Chem. Commun.* **2019**, *55*, 4731–4734.

[53] J. Hieulle, E. Carbonell-Sanromà, M. Vilas-Varela, A. Garcia-Lekue, E. Guitián, D. Peña, J. I. Pascual, *Nano Lett.* **2018**, *18*, 418–423.

[54] J. I. Mendieta-Moreno, B. Mallada, B. De la Torre, T. Cadart, M. Kotora, P. Jelínek, *Angew. Chem. Int. Ed.* **2022**, *61*, e202208010.

[55] P. Hapala, R. Temirov, F. S. Tautz, P. Jelínek, *Phys. Rev. Lett.* **2014**, *113*, 226101.

[56] F. Hanke, J. Björk, *Phys. Rev. B* **2013**, *87*, 235422.

[57] B. G. Hashiguchi, S. M. Bischof, M. M. Konnick, R. A. Periana, *Acc. Chem. Res.* **2012**, *45*, 885–898.

[58] J. Wencel-Delord, F. Glorius, *Nat. Chem.* **2013**, *5*, 369–375.

[59] B. Lowe, J. Hellerstedt, A. Matěj, P. Mutombo, D. Kumar, M. Ondráček, P. Jelinek, A. Schiffrin, *J. Am. Chem. Soc.* **2022**, *144*, 21389–21397.

[60] E. Darve, A. Pohorille, *J. Chem. Phys.* **2001**, *115*, 9169–9183.

[61] A. Kinikar, M. Di Giovannantonio, J. I. Urgel, K. Eimre, Z. Qiu, Y. Gu, E. Jin, A. Narita, X.-Y. Wang, K. Müllen, P. Ruffieux, C. A. Pignedoli, R. Fasel, *Nat. Synth.* **2022**, *1*, 289–296.

[62] F. Wu, A. Barragán, A. Gallardo, L. Yang, K. Biswas, D. Écija, J. I. Mendieta-Moreno, J. I. Urgel, J. Ma, X. Feng, *Chem. Eur. J.* **2023**, *29*, e202301739.

[63] I. Marcos-Alcalde, J. Setoain, J. I. Mendieta-Moreno, J. Mendieta, P. Gómez-Puertas, *Bioinformatics* **2015**, *31*, 3853–3855.

[64] F. Wu, A. Barragán, A. Gallardo, L. Yang, K. Biswas, D. Écija, X. Feng, *Chem. Eur. J.* **2023**, *29*(51), e202301739.